mater.scichina.com link.springer.com

Published online 10 December 2021 | https://doi.org/10.1007/s40843-021-1835-8
Sci China Mater 2022, 65(5): 1269–1275

Helical copper-porphyrinic framework nanoarrays for highly efficient CO_2 electroreduction

Yi-Hong Xiao[1,3], Yu-Xiang Zhang[4], Rui Zhai[1], Zhi-Gang Gu[1,2,3*] and Jian Zhang[1,2,3]

ABSTRACT **In recent years, metal-organic frameworks (MOFs) have been extensively investigated as electrocatalysts due to their highly efficient electroreduction of CO_2. Herein, the electrocatalytic CO_2 reduction reaction was investigated by growing helical Cu-porphyrinic MOF Cu meso-*tetra*(4-carboxyphenyl)porphyrin (TCPP) on $Cu(OH)_2$ nanoarrays (H-CuTCPP@$Cu(OH)_2$) using a sacrificial template method. The electrocatalytic results showed that the H-CuTCPP@$Cu(OH)_2$ nanoarrays exhibited a high acetic acid Faradaic efficiency (FE) of 26.1% at −1.6 V *vs.* Ag/Ag^+, which is much higher than the value of 19.8% obtained for non-helical CuTCPP@$Cu(OH)_2$ (nH-CuTCPP@$Cu(OH)_2$). The higher efficiency may be because space was more effectively utilized in the helical MOF nanoarrays, resulting in a greater number of active catalytic sites. Furthermore, *in situ* diffuse reflectance infrared Fourier transform spectra showed that the H-CuTCPP@$Cu(OH)_2$ nanoarrays have much stronger CO linear adsorption, indicating a better selectivity of acetic acid than that of nH-CuTCPP@$Cu(OH)_2$. In this study, we develop new helical nanomaterials and propose a new route to enhance the reduction of CO_2.**

Keywords: metal-organic framework, helical nanoarrays, CO_2 electroreduction

INTRODUCTION

The electrocatalytic CO_2 reduction is a prospective strategy for the transformation of CO_2 into fuels and chemicals. In this strategy, CO_2 is used as a raw material to produce valuable products, which can reduce greenhouse gas CO_2 and greatly contribute to solving environmental and energy crises [1–5]. With CO_2 electroreduction, it is usually more difficult to transform multi-carbon products than simple C_1 products [6–8]. Low C–C coupling activities in value-added C_{2+} products create difficulty during transformation, resulting in low efficiency [9–13]. To date, various electrocatalysts, such as metallic materials (e.g., Cu, Ni, Pd, Ag, and In components) [14–18], carbon-based materials [19–21], and organic-inorganic hybrid materials [22–24], have been designed to obtain high selectivity and activity for multi-carbon reduction products.

Metal-organic frameworks (MOFs), assembled from metal ions/clusters and organic ligands, are a type of crystalline porous material with diverse topological structure, high specific surface area, and tunable functionalities [25–28]. In the past decade, MOFs have been a popular research topic in the field of the electrocatalytic CO_2 reduction reaction (CO_2RR) due to their unsaturated active sites and porous structures [29–34]. Furthermore, great efforts have been made to enhance the selectivity of value-added products by optimizing MOF morphologies, grain boundaries, defects, etc. [35–39]. Particularly, MOFs or MOF-derived materials with different shapes, such as nanoparticles, nanosheets, and nanowires, have been proven to play a significant role in CO_2RR performance [40–44]. Recently, helical nanomaterials have improved the electrocatalytic performance, e.g., helical cobalt-doped carbonaceous nanotubes for oxygen reduction [45], helical metal borophosphates for water-splitting [46], and helical nitrogen-doped carbon nanotubes for metal-air batteries [47]. However, helical MOF nanomaterials have not been reported for electrocatalytic CO_2RR, which leaves a gap in energy conversion applications and offers a new route to further expand their functionalities.

In this study, we produced porphyrinic Cu-MOF helical nanosheets on the as-prepared $Cu(OH)_2$ nanoarrays to enhance CO_2 electroreduction. As shown in Fig. 1, $Cu(OH)_2$ nanoarrays were prepared on a Cu foil surface using an electrodeposition method [48,49]. Then, the $Cu(OH)_2$ nanoarrays were immersed into meso-*tetra*(4-carboxyphenyl)porphyrin (TCPP), and a porphyrin ligand was used to anchor the metal catalytic sites to aid charge transfer. The choice of *N*,*N*-dimethylformamide (DMF) solution and appropriate immersion time and temperature resulted in helical CuTCPP@$Cu(OH)_2$ nanoarrays (named H-CuTCPP@$Cu(OH)_2$). Due to synergistic effects from the Cu-porphyrin catalytic sites, high surface area, and the nano-helical structure, the acetic acid Faradaic efficiency (FE) of H-CuTCPP@$Cu(OH)_2$ was 26.1% at −1.6 V *vs.* Ag/Ag^+, which was much better than the FE value of 19.8% for non-helical CuTCPP@$Cu(OH)_2$ (Fig. S1, referred to as nH-CuTCPP@$Cu(OH)_2$). In addition, *in situ* diffuse reflectance infrared Fourier transform (DRIFT) spectra showed that the H-CuTCPP@$Cu(OH)_2$ nanoarrays had stronger CO linear adsorption, demonstrating better acetic acid selectivity than nH-CuTCPP@$Cu(OH)_2$. The results revealed that the helical structure of CuTCPP@$Cu(OH)_2$ could capture more CO intermediates, which effectively enhances acetic acid conversion to CO_2RR. This study presents novel helical electrocatalyst nano-

[1] State Key Laboratory of Structural Chemistry, Fujian Institute of Research on the Structure of Matter, Chinese Academy of Sciences, Fuzhou 350002, China
[2] Fujian Science & Technology Innovation Laboratory for Optoelectronic Information of China, Fuzhou 350108, China
[3] University of Chinese Academy of Sciences, Beijing 100049, China
[4] College of Physics and Energy, Fujian Normal University, Fuzhou 350117, China
* Corresponding author (email: zggu@fjirsm.ac.cn)

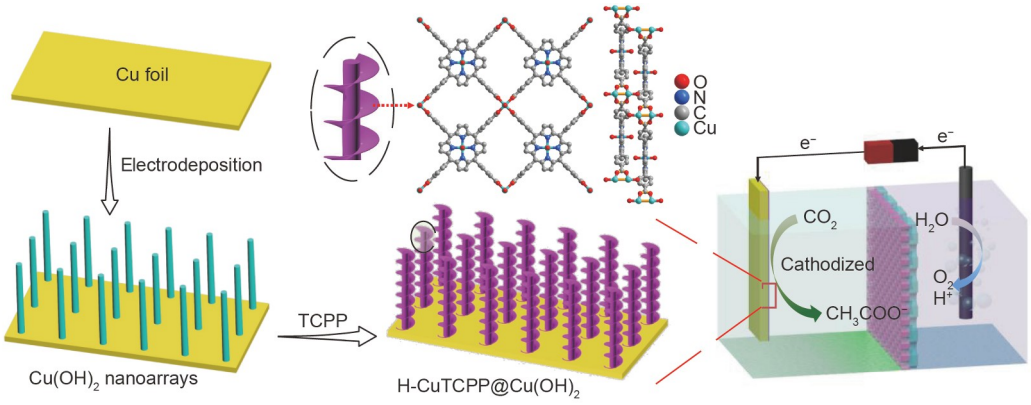

Figure 1 Process diagram for the fabrication of helical CuTCPP nanosheets on $Cu(OH)_2$ nanoarrays for CO_2 electroreduction.

materials and provides a new route for improving the electrocatalytic CO_2RR.

EXPERIMENTAL SECTION

Preparation of $Cu(OH)_2$ nanoarrays

In a two-electrode electrochemical cell, 0.1-mm-thick polycrystalline Cu foil (Alfa Aesar, 99.9999%) was used as the working electrode, and a platinum plate was used as the counter electrode. First, the Cu foil was ultrasonicated and pre-treated with a solution of 2 mol L^{-1} HCl, ethanol, and water for 5 min. The Cu foil and platinum plate were maintained at a distance of ~2 cm apart. Subsequently, Cu foil was anodized with a constant current condition (10 mA cm^{-2}) in 2 mol L^{-1} KOH (Sigma-Aldrich) aqueous electrolyte. After depositing for 400 s, the sample was washed with water and dried in a vacuum oven to obtain $Cu(OH)_2$ nanoarrays on the substrate surface.

Preparation of H-CuTCPP@$Cu(OH)_2$ nanoarrays

The as-prepared $Cu(OH)_2$ nanoarrays were immersed into TCPP in DMF solution (15 mg in 100 mL) at 80°C for 20 min and then washed with DMF to remove the unreacted TCPP ligands. After repeating this immersion growth for five cycles, the sample was soaked in acetone for 6 h and dried in a vacuum oven to obtain H-CuTCPP@$Cu(OH)_2$ nanoarrays.

Preparation of nH-CuTCPP@$Cu(OH)_2$ nanoarrays

First, 20 mg of $Cu(NO_3)_2$ and 15 mg of TCPP were dissolved in 100 mL of DMF, respectively. The as-prepared $Cu(OH)_2$ nanoarrays were then continuously immersed into TCPP and $Cu(NO_3)_2$ solutions at 80°C for 20 min; the film was washed with DMF after each step. A total of three growth cycles were performed to obtain nH-CuTCPP@$Cu(OH)_2$ nanoarrays. Finally, the sample was soaked in acetone for 6 h and dried in a vacuum oven.

Electrochemical measurements

Electrochemical measurements were carried out in a three-electrode system (typical H-type cell) on a CHI760E electrochemical workstation at room temperature. The experiments were carried out in an electrolyte of 0.5 mol L^{-1} 1-ethyl-3-methylimidazolium tetrafluoroborate ($EMIMBF_4$, 98%, Energy Chemical) acetonitrile (MeCN) solution with 1 mol L^{-1} H_2O, following the reported literature [50]. The electrolyte was pre-saturated with high purity Ar or CO_2 for about 30 min before each test. Typically, the samples were utilized as the working electrode, a Ag/Ag^+ electrode (filled with 0.01 mol L^{-1} $AgNO_3$ MeCN solution) was used as the reference electrode, and platinum foil was used as the counter electrode. Before recording the linear sweep voltammetry (LSV) curves, several cyclic voltammetry cycles at a sweep rate of 50 mV s^{-1} were taken to stabilize their CO_2RR properties. LSV curves were recorded in the potential range of −0.5 to −2 V *vs.* Ag/Ag^+ at a scanning rate of 5 mV s^{-1}. During the electrocatalytic measurements, the electrolyte was continuously bubbled with CO_2 (at a flow rate of 10 mL min^{-1}) to form a saturated solution. The measurement was performed at selected potentials (chronoamperometry) for 5 h to determine the reduction products and FEs of the electrocatalysts.

RESULTS AND DISCUSSION

Preparation and characterization

First, $Cu(OH)_2$ nanoarrays were prepared by the electrodeposition method on the Cu foil surface and anodized with 10 mA cm^{-2} in 2 mol L^{-1} KOH solution. The X-ray diffraction (XRD) pattern (Fig. 2a) of $Cu(OH)_2$ was identical to the standard PDF card #80-0656, indicating that $Cu(OH)_2$ was successfully fabricated on the Cu foil surface. XRD measurements were carried out again after $Cu(OH)_2$ nanoarrays underwent the final process for forming H-CuTCPP@$Cu(OH)_2$. The XRD pattern (Fig. 2a) indicated that a portion of $Cu(OH)_2$ reacted with TCPP ligands, and CuTCPP was successfully grown on the $Cu(OH)_2$ surface. Infrared (IR) spectra (Fig. 2b) also revealed the existence of a hydroxyl group and that the carbonyl stretching vibrations disappeared in CuTCPP@$Cu(OH)_2$, suggesting that Cu^{2+} coordinated with TCPP on the $Cu(OH)_2$ surface. The ultraviolet-visible (UV-vis) absorption spectra of H-CuTCPP@$Cu(OH)_2$ (Fig. 2c) revealed much weaker intensity and a slight redshift of three Q-bands compared with the four Q-bands of TCPP, indicating that TCPP was metalated during the process. The X-ray photoelectron spectroscopy (XPS) data (Fig. S2) also demonstrated that the center of the porphyrin group in H-CuTCPP@$Cu(OH)_2$ was successfully metalized with Cu that was provided by the $Cu(OH)_2$ nanoarrays [51]. Furthermore, atomic force microscopy images (Fig. S3) showed that the CuTCPP nanosheets had a thickness of ~7 nm.

As shown in Fig. S4, $Cu(OH)_2$ was electrodeposited on Cu foil

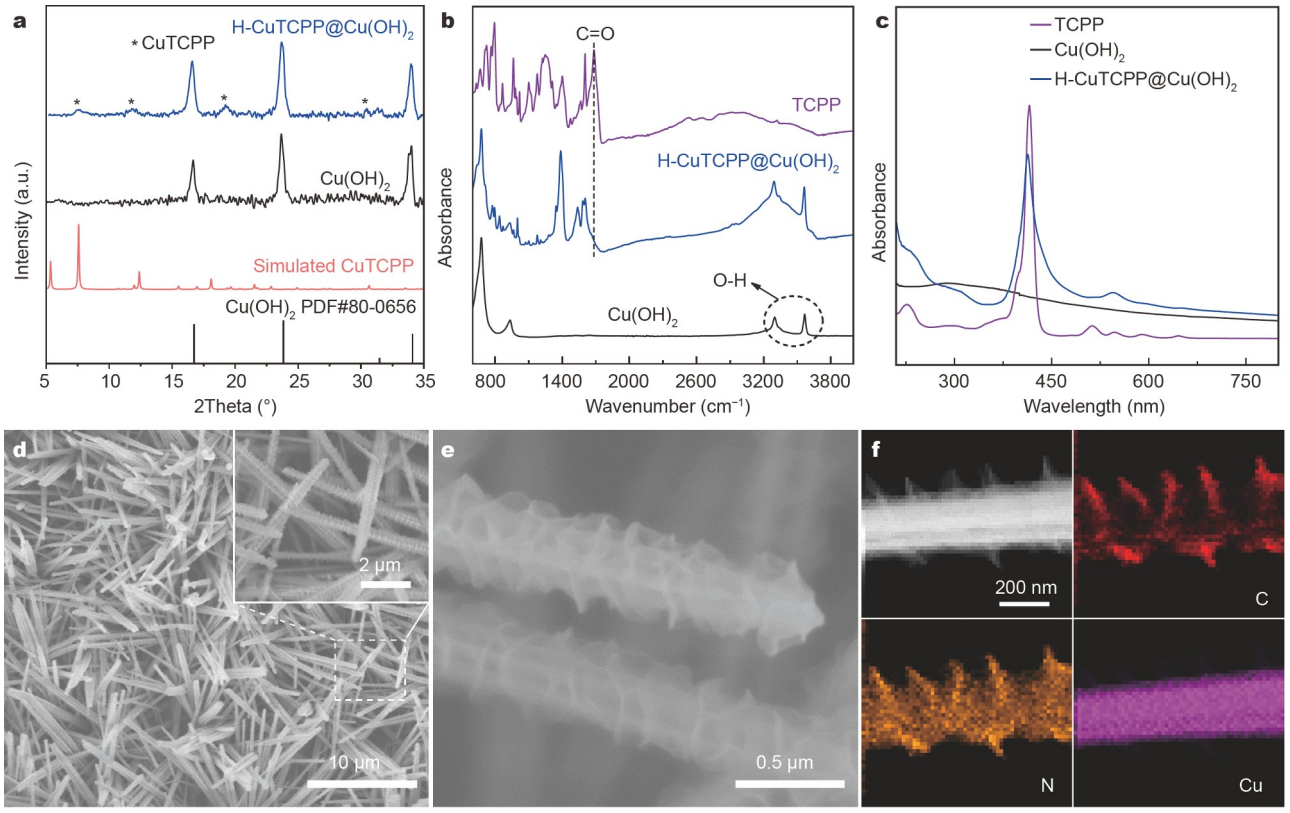

Figure 2 (a) XRD patterns of $Cu(OH)_2$ and H-CuTCPP@$Cu(OH)_2$ nanoarrays; (b) IR and (c) UV-vis spectra of TCPP, $Cu(OH)_2$, and H-CuTCPP@$Cu(OH)_2$ nanoarrays; (d, e) SEM images of H-CuTCPP@$Cu(OH)_2$ nanoarrays; (f) TEM element mapping of H-CuTCPP@$Cu(OH)_2$ nanoarrays.

(Fig. S5) to produce uniform nanoarrays with a diameter of ~500 nm. The nanowire nanomaterials exist due to the phenomenon of screw dislocations and the associated Eshelby twist, without any chiral resources, which provide self-perpetuating step edges of nanowires and break the growth symmetry [52–55]. The as-prepared $Cu(OH)_2$ nanowires were then used as sacrificial templates (direct metal source) with screw dislocation features [56] to react with appropriate concentrations of TCPP solutions, promoting a helical CuTCPP on the surface of $Cu(OH)_2$ (Fig. 2d, e). Since chiral resources were not introduced in the synthesis process, only mono-chiral helical CuTCPP was formed under the conditions, and it was not possible to obtain another enantiomeric CuTCPP.

For comparison, the as-prepared $Cu(OH)_2$ nanoarrays were subsequently immersed in TCPP and $Cu(NO_3)_2$ DMF solutions over three cycles and washed with DMF after each step. A core-shell CuTCPP@$Cu(OH)_2$ with non-helical structure (namely nH-CuTCPP@$Cu(OH)_2$) was thus produced on the Cu foil as the external Cu source in the liquid-phase epitaxy process broke the ordered twist. The XRD pattern and scanning electron microscopy (SEM) images of this material are shown in Figs S6 and S7, respectively. It was obvious that the CuTCPP nanosheets of H-CuTCPP@$Cu(OH)_2$ were much thinner than those of nH-CuTCPP@$Cu(OH)_2$ because external Cu sources were not used. Moreover, the shape and element distributions were characterized using the transmission electron microscopy (TEM) and electron energy loss spectroscopy (EELS) element mapping shown in Fig. S8 and Fig. 2f. The well-distributed C, N, O, and Cu elements in H-CuTCPP@$Cu(OH)_2$ demonstrated that helical CuTCPP nanosheets were homogeneously grown on the surface of $Cu(OH)_2$. In addition, the TEM-EELS line scan data (Fig. S9) of H-CuTCPP@$Cu(OH)_2$ showed uniformly distributed elements, with the element content in the middle being higher than that on both sides. This demonstrates that the CuTCPP nanosheets were wrapped on the surface of the $Cu(OH)_2$ nanoarrays.

Chiral properties

The chiral properties of the helical CuTCPP nanosheets homogeneously distributed on the $Cu(OH)_2$ surface were studied. The circular dichroism (CD) spectra (Fig. 3) showed that H-CuTCPP@$Cu(OH)_2$ produced an obvious chiral signal with a negative band at ~430 nm. On the contrary, nH-CuTCPP@$Cu(OH)_2$ and bare $Cu(OH)_2$ nanoarrays did not show any chiral signals, nor did any pure TCPP ligands and CuTCPP powder (Fig. S10). This result suggested that all the raw materials did not have any chirality. In addition, H-CuTCPP@$Cu(OH)_2$ was immersed in an alkaline solution to remove the helical distributed CuTCPP nanosheets and obtained residual $Cu(OH)_2$ (Fig. S11). As can be seen in Fig. S10, a CD signal was not observed, which indicated that the chirality of CuTCPP was not induced by $Cu(OH)_2$. These CD spectra suggested that the different shapes of CuTCPP on the $Cu(OH)_2$ nanoarrays play a significant role in chiral induction.

CO_2RR performance

Cu-based materials are promising electrocatalysts in CO_2RR [57–59]. To investigate the CO_2RR performance of helical CuTCPP, H-CuTCPP@$Cu(OH)_2$, nH-CuTCPP-$Cu(OH)_2$, and $Cu(OH)_2$ nanoarrays were investigated using a three-electrode

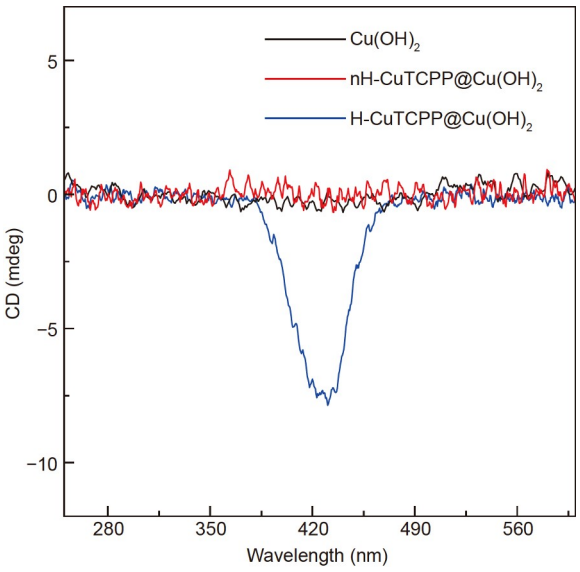

Figure 3 Circular dichroism spectra of $Cu(OH)_2$, nH-CuTCPP@$Cu(OH)_2$, and H-CuTCPP@$Cu(OH)_2$ nanoarrays.

system. The LSV curve (Fig. S12a) of the H-CuTCPP@$Cu(OH)_2$ nanoarrays showed that the current density continuously increased, starting from an onset potential of −1.2 V *vs.* Ag/Ag^+ in the CO_2-saturated electrolyte, which was higher than that in the Ar-saturated electrolyte. This suggests that the H-CuTCPP@$Cu(OH)_2$ nanoarrays can reduce CO_2. Similarly, the nH-CuTCPP@$Cu(OH)_2$ and $Cu(OH)_2$ nanoarrays exhibited CO_2 reduction capacity, as can be seen in the LSV curves in Fig. S12b, c. The samples were electrolyzed at different potentials, between −1.4 and −1.8 V *vs.* Ag/Ag^+ for 5 h, and the CO_2RR products were collected. The current densities of H-CuTCPP@$Cu(OH)_2$, nH-CuTCPP@$Cu(OH)_2$, and $Cu(OH)_2$ nanoarrays were recorded at different potentials (Fig. 4a), further examined by gas chromatography, and quantitatively analyzed by ^1H nuclear magnetic resonance spectroscopy.

As shown in Figs S13 and S14, a small amount of CO and H_2 gaseous products from the H-CuTCPP@$Cu(OH)_2$, nH-CuTCPP@$Cu(OH)_2$, and $Cu(OH)_2$ nanoarrays were detected; they had low FE. Thus, the liquid-phase products were further tested, and the existence of formic and acetic acids was confirmed. Calibration curves for the products were obtained by measuring the standard solutions (Figs S15 and S16). The FEs of formic acid for the H-CuTCPP@$Cu(OH)_2$, nH-CuTCPP@$Cu(OH)_2$ and $Cu(OH)_2$ nanoarrays at different potentials (Fig. 4b) showed that both H-CuTCPP@$Cu(OH)_2$ and nH-CuTCPP@$Cu(OH)_2$ had the highest FE with ~35.0% at a potential of −1.7 V *vs.* Ag/Ag^+. The FE of the bare $Cu(OH)_2$ nanoarrays was ~26.6% at a potential of −1.5 V *vs.* Ag/Ag^+. The FE of acetic acid for the H-CuTCPP@$Cu(OH)_2$ nanoarrays increased to a maximum value of 26.1% at −1.6 V *vs.* Ag/Ag^+, which was higher than that of nH-CuTCPP@$Cu(OH)_2$ (19.8%)

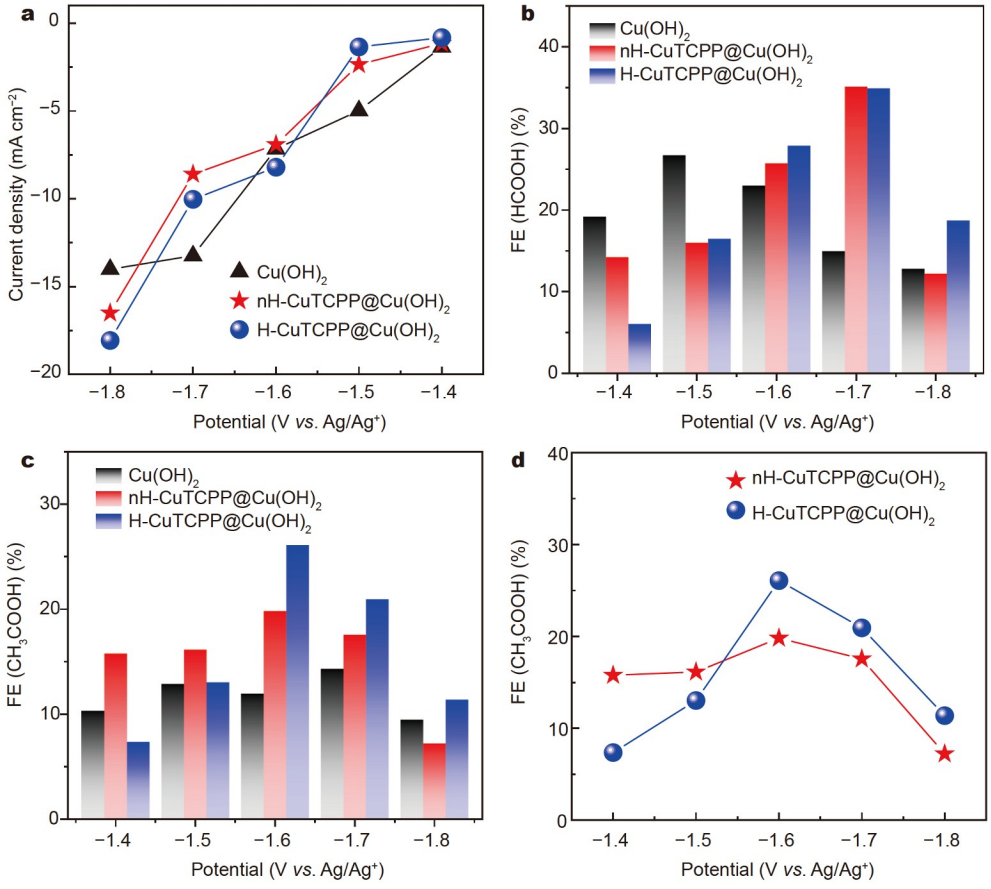

Figure 4 (a) Current densities of H-CuTCPP@$Cu(OH)_2$, nH-CuTCPP@$Cu(OH)_2$, and $Cu(OH)_2$ nanoarrays at different potentials; FEs of (b) formic acid and (c, d) acetic acid for $Cu(OH)_2$, nH-CuTCPP@$Cu(OH)_2$, and H-CuTCPP@$Cu(OH)_2$ nanoarrays.

and $Cu(OH)_2$ nanoarrays (12.0%) at the same potential (Fig. 4c). The H-CuTCPP@$Cu(OH)_2$ and nH-CuTCPP@$Cu(OH)_2$ nanoarrays were further analyzed for the more value-added acetic acid. As shown in Fig. 4d, the acetic acid FE of the H-CuTCPP@$Cu(OH)_2$ nanoarrays was much lower than that of nH-CuTCPP@Cu-$(OH)_2$ at the first two potentials. A possible explanation for this result is that the compact and higher surface area of nH-CuTCPP@$Cu(OH)_2$ had a significant impact at lower potentials. However, the H-CuTCPP@$Cu(OH)_2$ nanoarrays quickly reached the highest acetic acid FE at −1.6 V *vs.* Ag/Ag^+, which is much higher than that of nH-CuTCPP@$Cu(OH)_2$ from −1.6 to −1.8 V *vs.* Ag/Ag^+. In addition, the stability of the current over time was recorded and displayed by current density-time (*i-t*) curves (Fig. S17). The results demonstrated that CuTCPP@$Cu(OH)_2$ with helical nanoarrays was highly efficient for reducing CO_2 to acetic acid.

To further analyze the selectivity of acetic acid on the obtained electrocatalysts, *in situ* DRIFT spectra of CO adsorption and desorption were tested for the electrocatalysts. This was done since CO was an intermediate for the formation of acetic acid and was not involved in the formation of formic acid. The *in situ* DRIFT spectra (Fig. 5a) of CO adsorption on the H-CuTCPP@$Cu(OH)_2$ nanoarrays revealed strong peaks at ~2118 and ~2170 cm^{-1}, which were attributed to CO physisorption; the CO adsorption value reached saturation immediately. Importantly, two peaks at ~1998 and ~2018 cm^{-1} were assigned to CO linear adsorption [60], and the intensity of the peaks gradually increased as time increased from 5 to 50 min. The *in situ* DRIFT spectra of CO desorption for the H-CuTCPP@$Cu(OH)_2$ nanoarrays displayed both CO physisorption and linear adsorption, which gradually decreased as time increased from 2 to 30 min (Fig. 5b). Similarly, the nH-CuTCPP@$Cu(OH)_2$ nanoarrays exhibited the same properties (Figs S18 and S19). This indicated that the surfaces of H-CuTCPP@$Cu(OH)_2$ and nH-CuTCPP@$Cu(OH)_2$ nanoarrays could not only physically adsorb CO, but also chemically coordinate with CO [61], which was helpful for the participation of CO in acetic acid formation. The intensity of CO linear adsorption on H-CuTCPP@$Cu(OH)_2$ for 50 min was slightly higher than that of nH-CuTCPP@$Cu(OH)_2$ (Fig. 5c). In the desorption process, H-CuTCPP@$Cu(OH)_2$ also had more CO linear adsorption than nH-CuTCPP@$Cu(OH)_2$ at 2 or 30 min (Fig. 5d and Fig. S20). Moreover, in order to eliminate the influence of the different sizes, a thinner and smaller nH-CuTCPP(t)@$Cu(OH)_2$ was prepared. SEM images (Fig. S21) and CD spectrum (Fig. S22) demonstrated successful preparation of the nH-CuTCPP(t)@$Cu(OH)_2$ nanoarrays. The *in situ* DRIFT spectra of CO adsorption and desorption on the nH-CuTCPP(t)@$Cu(OH)_2$ nanoarrays showed that the intensity of CO physical adsorption and linear adsorption was close to that of nH-CuTCPP@$Cu(OH)_2$, both of which were much smaller than that of H-CuTCPP@$Cu(OH)_2$ (Figs S23–S25). The electrocatalytic

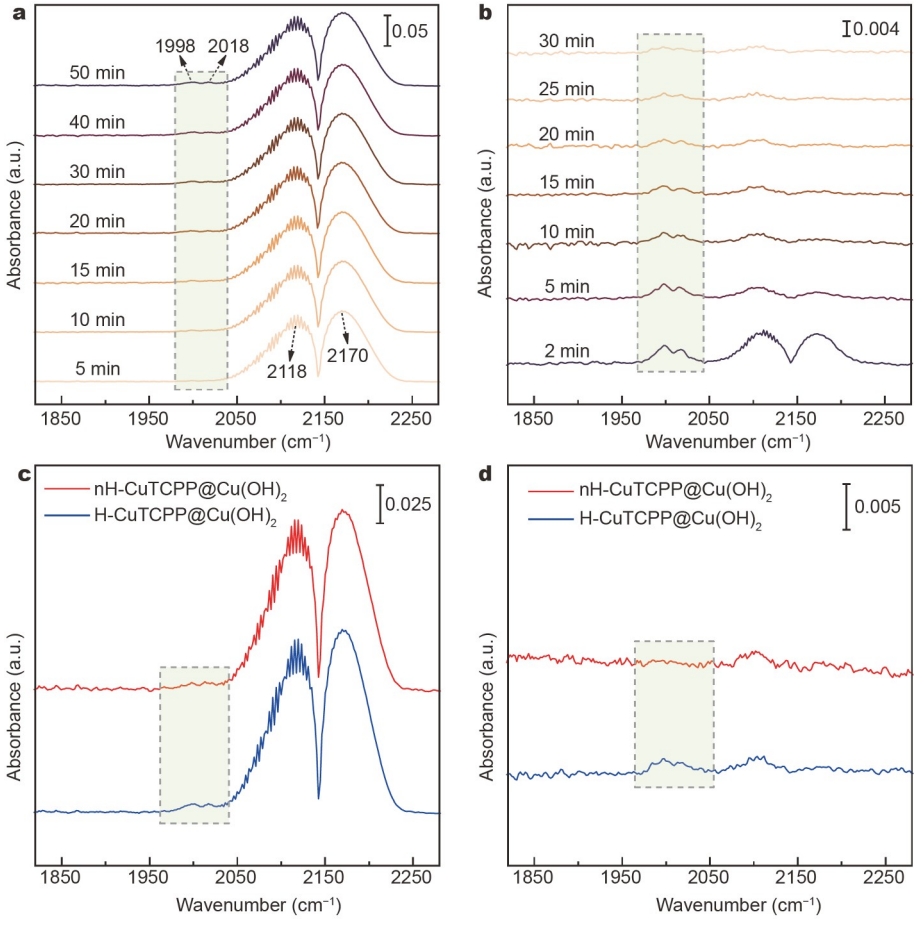

Figure 5 *In situ* DRIFT spectra of CO (a) adsorption from 5 to 50 min and (b) desorption from 2 to 30 min of H-CuTCPP@$Cu(OH)_2$ nanoarrays; *in situ* DRIFT spectra of CO (c) adsorption at 50 min and (d) desorption at 30 min for nH-CuTCPP@$Cu(OH)_2$ and H-CuTCPP@$Cu(OH)_2$ nanoarrays.

reduction of CO_2 to acetic acid was also much lower than that of H-CuTCPP@$Cu(OH)_2$ (Fig. S26). Therefore, the H-CuTCPP@$Cu(OH)_2$ nanoarrays exhibited much stronger CO linear adsorption, indicating that more CO was involved in the formation of acetic acid, which may be attributed to the homogenous helical structure of CuTCPP. In addition, XRD, SEM, and XPS (Figs S27–S29) were used to analyze the electrocatalysts after electrolysis. It was revealed that CuTCPP played a crucial role in electrocatalytic performance [50]. The results indicated that that anchoring helical CuTCPP on the $Cu(OH)_2$ nanoarrays could improve the electrocatalytic activity of the C_2 product.

CONCLUSIONS

In summary, we developed helical MOF CuTCPP attached on the surface of $Cu(OH)_2$ nanoarrays for enhancing the electrocatalytic CO_2RR to acetic acid. The $Cu(OH)_2$ nanoarrays were fabricated on Cu foil using the electrodeposition method. The nanoarrays then acted as a sacrificial template, and chiral H-CuTCPP@$Cu(OH)_2$ nanoarrays were assembled on the surfaces through immersion in a TCPP solution. The electrocatalytic results showed that the H-CuTCPP@$Cu(OH)_2$ nanoarrays exhibited a high acetic acid FE of 26.1% at a potential of −1.6 V *vs*. Ag/Ag^+, which was much higher than that of nH-CuTCPP@$Cu(OH)_2$ (19.8%). Moreover, *in situ* DRIFT spectra demonstrated that the H-CuTCPP@$Cu(OH)_2$ nanoarrays had much stronger CO linear adsorption, resulting in the improved conversion of CO_2 to acetic acid. This finding demonstrates that helical porphyrinic MOF nanoarrays provide new candidates for the enhancement of CO_2 electroreduction to multi-carbon products.

Received 1 September 2021; accepted 19 October 2021; published online 10 December 2021

1 Dinh CT, Burdyny T, Kibria MG, *et al.* CO_2 electroreduction to ethylene *via* hydroxide-mediated copper catalysis at an abrupt interface. Science, 2018, 360: 783–787
2 Zhang W, Hu Y, Ma L, *et al.* Progress and perspective of electrocatalytic CO_2 reduction for renewable carbonaceous fuels and chemicals. Adv Sci, 2018, 5: 1700275
3 Wu Y, Zhai P, Cao S, *et al.* Beyond d orbits: Steering the selectivity of electrochemical CO_2 reduction *via* hybridized sp band of sulfur-incorporated porous Cd architectures with dual collaborative sites. Adv Energy Mater, 2020, 10: 2002499
4 Zhang N, Long R, Gao C, *et al.* Recent progress on advanced design for photoelectrochemical reduction of CO_2 to fuels. Sci China Mater, 2018, 61: 771–805
5 Wang X, Sang X, Dong CL, *et al.* Proton capture strategy for enhancing electrochemical CO_2 reduction on atomically dispersed metal-nitrogen active sites. Angew Chem Int Ed, 2021, 60: 11959–11965
6 Jouny M, Luc W, Jiao F. High-rate electroreduction of carbon monoxide to multi-carbon products. Nat Catal, 2018, 1: 748–755
7 Wu ZZ, Gao FY, Gao MR. Regulating the oxidation state of nanomaterials for electrocatalytic CO_2 reduction. Energy Environ Sci, 2021, 14: 1121–1139
8 Wu Y, Cao S, Hou J, *et al.* Rational design of nanocatalysts with nonmetal species modification for electrochemical CO_2 reduction. Adv Energy Mater, 2020, 10: 2000588
9 Pei W, Zhou S, Zhao J, *et al.* Immobilized trimeric metal clusters: A family of the smallest catalysts for selective CO_2 reduction toward multi-carbon products. Nano Energy, 2020, 76: 105049
10 Wang X, Wang Z, Zhuang TT, *et al.* Efficient upgrading of CO to C_3 fuel using asymmetric C–C coupling active sites. Nat Commun, 2019, 10: 5186
11 Handoko AD, Wei F, Jenndy F, *et al.* Understanding heterogeneous electrocatalytic carbon dioxide reduction through operando techniques. Nat Catal, 2018, 1: 922–934
12 Jung H, Lee SY, Lee CW, *et al.* Electrochemical fragmentation of Cu_2O nanoparticles enhancing selective C–C coupling from CO_2 reduction reaction. J Am Chem Soc, 2019, 141: 4624–4633
13 Chen J, Wang T, Li Z, *et al.* Recent progress and perspective of electrochemical CO_2 reduction towards C_2-C_5 products over non-precious metal heterogeneous electrocatalysts. Nano Res, 2021, 14: 3188–3207
14 Raciti D, Wang C. Recent advances in CO_2 reduction electrocatalysis on copper. ACS Energy Lett, 2018, 3: 1545–1556
15 Zhang X, Liu C, Zhao Y, *et al.* Atomic nickel cluster decorated defect-rich copper for enhanced C_2 product selectivity in electrocatalytic CO_2 reduction. Appl Catal B-Environ, 2021, 291: 120030
16 He J, Johnson NJJ, Huang A, *et al.* Electrocatalytic alloys for CO_2 reduction. ChemSusChem, 2018, 11: 48–57
17 Zhang Q, Tao S, Du J, *et al.* A cold plasma-activated *in situ* AgCo surface alloy for enhancing the electroreduction of CO_2 to ethanol. J Mater Chem A, 2020, 8: 8410–8420
18 Zha B, Li C, Li J. Efficient electrochemical reduction of CO_2 into formate and acetate in polyoxometalate catholyte with indium catalyst. J Catal, 2020, 382: 69–76
19 Zhao K, Quan X. Carbon-based materials for electrochemical reduction of CO_2 to C_{2+} oxygenates: Recent progress and remaining challenges. ACS Catal, 2021, 11: 2076–2097
20 Wu J, Ma S, Sun J, *et al.* A metal-free electrocatalyst for carbon dioxide reduction to multi-carbon hydrocarbons and oxygenates. Nat Commun, 2016, 7: 13869
21 Vasileff A, Zheng Y, Qiao SZ. Carbon solving carbon's problems: Recent progress of nanostructured carbon-based catalysts for the electrochemical reduction of CO_2. Adv Energy Mater, 2017, 7: 1700759
22 Nam DH, Bushuyev OS, Li J, *et al.* Metal-organic frameworks mediate Cu coordination for selective CO_2 electroreduction. J Am Chem Soc, 2018, 140: 11378–11386
23 Yang C, Li S, Zhang Z, *et al.* Organic-inorganic hybrid nanomaterials for electrocatalytic CO_2 reduction. Small, 2020, 16: 2001847
24 Wang Y, Li Y, Wang Z, *et al.* Reticular chemistry in electrochemical carbon dioxide reduction. Sci China Mater, 2020, 63: 1113–1141
25 Zhou HC, Long JR, Yaghi OM. Introduction to metal-organic frameworks. Chem Rev, 2012, 112: 673–674
26 Cui Y, Li B, He H, *et al.* Metal-organic frameworks as platforms for functional materials. Acc Chem Res, 2016, 49: 483–493
27 Zhou HC, Kitagawa S. Metal-organic frameworks (MOFs). Chem Soc Rev, 2014, 43: 5415–5418
28 Chen L, Luque R, Li Y. Controllable design of tunable nanostructures inside metal-organic frameworks. Chem Soc Rev, 2017, 46: 4614–4630
29 Liao PQ, Shen JQ, Zhang JP. Metal-organic frameworks for electrocatalysis. Coord Chem Rev, 2018, 373: 22–48
30 Xu Y, Li Q, Xue H, *et al.* Metal-organic frameworks for direct electrochemical applications. Coord Chem Rev, 2018, 376: 292–318
31 Li D, Xu HQ, Jiao L, *et al.* Metal-organic frameworks for catalysis: State of the art, challenges, and opportunities. EnergyChem, 2019, 1: 100005
32 Wu HB, Lou XWD. Metal-organic frameworks and their derived materials for electrochemical energy storage and conversion: Promises and challenges. Sci Adv, 2017, 3: eaap9252
33 Zhang Y, Guo SX, Zhang X, *et al.* Mechanistic understanding of the electrocatalytic CO_2 reduction reaction—New developments based on advanced instrumental techniques. Nano Today, 2020, 31: 100835
34 Sun T, Xu L, Wang D, *et al.* Metal organic frameworks derived single atom catalysts for electrocatalytic energy conversion. Nano Res, 2019, 12: 2067–2080
35 Yuan M, Wang R, Sun Z, *et al.* Morphology-controlled synthesis of Ni-MOFs with highly enhanced electrocatalytic performance for urea oxidation. Inorg Chem, 2019, 58: 11449–11457
36 Nam DH, Shekhah O, Lee G, *et al.* Intermediate binding control using metal-organic frameworks enhances electrochemical CO_2 reduction. J Am Chem Soc, 2020, 142: 21513–21521
37 Wang Y, Han P, Lv X, *et al.* Defect and interface engineering for aqueous electrocatalytic CO_2 reduction. Joule, 2018, 2: 2551–2582

38 Cheng H, Wu X, Li X, *et al.* Construction of atomically dispersed CuN_4 sites *via* engineered coordination environment for high-efficient CO_2 electroreduction. Chem Eng J, 2021, 407: 126842
39 Wang G, Chen J, Ding Y, *et al.* Electrocatalysis for CO_2 conversion: From fundamentals to value-added products. Chem Soc Rev, 2021, 50: 4993–5061
40 Zhang E, Wang T, Yu K, *et al.* Bismuth single atoms resulting from transformation of metal-organic frameworks and their use as electrocatalysts for CO_2 reduction. J Am Chem Soc, 2019, 141: 16569–16573
41 Zhu D, Qiao M, Liu J, *et al.* Engineering pristine 2D metal-organic framework nanosheets for electrocatalysis. J Mater Chem A, 2020, 8: 8143–8170
42 Yang F, Deng PL, Wang Q, *et al.* Metal-organic framework-derived cupric oxide polycrystalline nanowires for selective carbon dioxide electroreduction to C_2 valuables. J Mater Chem A, 2020, 8: 12418–12423
43 Li N, Yan P, Tang Y, *et al.* *In-situ* formation of ligand-stabilized bismuth nanosheets for efficient CO_2 conversion. Appl Catal B-Environ, 2021, 297: 120481
44 Wang X, Wang Y, Sang X, *et al.* Dynamic activation of adsorbed intermediates *via* axial traction for the promoted electrochemical CO_2 reduction. Angew Chem Int Ed, 2021, 60: 4192–4198
45 Liang Z, Fan X, Lei H, *et al.* Corrigendum: Cobalt-nitrogen-doped helical carbonaceous nanotubes as a class of efficient electrocatalysts for the oxygen reduction reaction. Angew Chem Int Ed, 2018, 57: 16593
46 Menezes PW, Indra A, Zaharieva I, *et al.* Helical cobalt borophosphates to master durable overall water-splitting. Energy Environ Sci, 2019, 12: 988–999
47 Liu Y, Wang B, Sun Q, *et al.* Controllable synthesis of Co@CoO_x/helical nitrogen-doped carbon nanotubes toward oxygen reduction reaction as binder-free cathodes for Al-air batteries. ACS Appl Mater Interfaces, 2020, 12: 16512–16520
48 Lee SY, Jung H, Kim NK, *et al.* Mixed copper states in anodized Cu electrocatalyst for stable and selective ethylene production from CO_2 reduction. J Am Chem Soc, 2018, 140: 8681–8689
49 Hou J, Cheng H, Takeda O, *et al.* Three-dimensional bimetal-graphene-semiconductor coaxial nanowire arrays to harness charge flow for the photochemical reduction of carbon dioxide. Angew Chem Int Ed, 2015, 54: 8480–8484
50 Wu JX, Hou SZ, Zhang XD, *et al.* Cathodized copper porphyrin metal-organic framework nanosheets for selective formate and acetate production from CO_2 electroreduction. Chem Sci, 2019, 10: 2199–2205
51 Guo X, Li X, Qin L, *et al.* A highly active nano-micro hybrid derived from Cu-bridged TiO_2/porphyrin for enhanced photocatalytic hydrogen production. Appl Catal B-Environ, 2019, 243: 1–9
52 Veblen DR, Post JE. A TEM study of fibrous cuprite (chalcotrichite)—Microstructures and growth mechanisms. Am Mineral, 1983, 68: 790–803
53 Eshelby JD. Screw dislocations in thin rods. J Appl Phys, 1953, 24: 176–179
54 Meng F, Morin SA, Forticaux A, *et al.* Screw dislocation driven growth of nanomaterials. Acc Chem Res, 2013, 46: 1616–1626
55 Meng F, Morin SA, Jin S. Rational solution growth of α-FeOOH nanowires driven by screw dislocations and their conversion to α-Fe_2O_3 nanowires. J Am Chem Soc, 2011, 133: 8408–8411
56 Shtukenberg AG, Punin YO, Gujral A, *et al.* Growth actuated bending and twisting of single crystals. Angew Chem Int Ed, 2014, 53: 672–699
57 Xie H, Wang T, Liang J, *et al.* Cu-based nanocatalysts for electrochemical reduction of CO_2. Nano Today, 2018, 21: 41–54
58 Chen Y, Fan Z, Wang J, *et al.* Ethylene selectivity in electrocatalytic CO_2 reduction on Cu nanomaterials: A crystal phase-dependent study. J Am Chem Soc, 2020, 142: 12760–12766
59 Zhao Y, Liu X, Chen D, *et al.* Atomic-level-designed copper atoms on hierarchically porous gold architectures for high-efficiency electrochemical CO_2 reduction. Sci China Mater, 2021, 64: 1900–1909
60 Chen YZ, Zhou YX, Wang H, *et al.* Multifunctional PdAg@MIL-101 for one-pot cascade reactions: Combination of host-guest cooperation and bimetallic synergy in catalysis. ACS Catal, 2015, 5: 2062–2069
61 Wang C, Chen P, Li Y, *et al.* *In situ* DRIFTS study of CO coupling to dimethyl oxalate over structured Al-fiber@ns-AlOOH@Pd catalyst. J Catal, 2016, 344: 173–183

Acknowledgements This work was supported by the National Key Research and Development Program of China (2018YFA0208600), the National Natural Science Foundation of China (21872148 and 21601189), the Youth Innovation Promotion Association of the Chinese Academy of Sciences (2018339) and Fujian Science & Technology Innovation Laboratory for Optoelectronic Information of China (2021ZR131).

Author contributions Xiao YH performed the experiments, analyzed the data, and wrote the manuscript draft under the guidance of Gu ZG and Zhang J; Zhang YX helped with the SEM measurements; Zhai R provided research suggestions. All authors contributed to the general discussion.

Conflict of interest The authors declare that they have no conflict of interest.

Supplementary information Experimental details and supporting data are available in the online version of the paper.

Yi-Hong Xiao received his BS degree in 2017 from Fujian Normal University. He is currently a PhD student under the supervision of Prof. Zhi-Gang Gu and Prof. Jian Zhang at Fujian Institute of Research on the Structure of Matter (FJIRSM), Chinese Academy of Sciences (CAS). His current research interests focus on the preparation and photo/electric properties of composite MOF films.

Zhi-Gang Gu obtained his PhD degree from Karlsruhe Institute of Technology (KIT) in 2014 and then worked as a postdoctoral fellow at KIT. In 2015 he became an associate professor, and in 2018 he was promoted to a professor at FFJIRSM, CAS. His recent research focuses on the controllable assembly and functionalities of surface-coordinated metal-organic framework thin films (SURMOFs).

螺旋铜-卟啉框架纳米阵列用于高效的二氧化碳电还原

肖义鈜[1,3], 张裕祥[4], 翟瑞[1], 谷志刚[1,2,3*], 张健[1,2,3]

摘要 金属-有机框架(MOF)因其高的比表面积、可调的孔道结构等特点, 近年来在电催化二氧化碳还原领域受到了广泛的关注. 本文中, 我们首次采用牺牲模板法在$Cu(OH)_2$纳米阵列上生长具有螺旋形貌的铜-卟啉基MOF CuTCPP (H-CuTCPP@$Cu(OH)_2$), 并研究了其电催化二氧化碳还原性能. 电催化性能显示, 在−1.6 V *vs.* Ag/Ag^+电势下, H-CuTCPP@$Cu(OH)_2$表现出二氧化碳还原成乙酸的高效性能, 其法拉第效率高达26.1%, 并优于非螺旋CuTCPP (nH-CuTCPP@$Cu(OH)_2$) (19.8%). 这是因为螺旋MOF纳米阵列具有更有效的催化空间并提供了更多催化活性位点. 此外, 原位红外光谱证实了H-CuTCPP@$Cu(OH)_2$对一氧化碳具有更强的线性吸附, 因此具有更高的乙酸选择性. 这项工作不仅开发了新型螺旋纳米材料, 也为提高电催化二氧化碳还原性能提供了一种新的途径.

